

## Spin angular momentum transfer in a current-perpendicular spin-valve nanomagnet

J. Z. Sun<sup>a</sup>, T. S. Kuan<sup>b</sup>, J. A. Katine<sup>c</sup>, and R. H. Koch<sup>a</sup>

<sup>a</sup>IBM T. J. Watson Research Center, PO Box 218, Yorktown Heights, NY 10598, USA

<sup>b</sup>Physics Department, University at Albany, SUNY, Albany NY 12222, USA

<sup>c</sup>IBM Almaden Research Center, 650 Harry Road, CA 95120, USA; Currently at Hitachi Global Storage Technologies, San Jose Research Center, 650 Harry Road, CA 95120, USA

### ABSTRACT

Spin-angular momentum transfer (or spin-transfer for short) describes the angular momentum exchange between a spin-polarized current and a ferromagnetic conductor. When the conductor dimensions are reduced to around 100nm or below, the spin-angular momentum transfer effect becomes significant compared to the current-induced magnetic field. This paper describes some recent spin-transfer experimental findings in sub-100nm current-perpendicular spin-valve systems consisting of Co-Cu-Co nanopillars. The spin-transfer current is shown to cause a magnetic reversal of the thinner magnetic layer inside the nanopillar. The reversal is experimentally shown to reach sub-nanosecond speed. The effect of spin-transfer is best understood in terms of its modification to the effective Landau-Lifshitz-Gilbert damping coefficient, either increasing or decreasing its value depending on the direction and magnitude of the spin-polarized current. For sufficiently large spin-current, the net damping coefficient may change sign, resulting in amplification of magnetic precession, leading to a magnetic reversal. At finite temperatures, the effect of spin-transfer is to either increase or decrease the thermal agitation of the nanomagnet. A quantitative model is developed that adequately describes the finite temperature experimental observations of the dynamic spin-transfer effect.

**Keywords:** spin-transfer, magnetic nanostructures, spin-valve, finite temperature

### 1. INTRODUCTION

Spin-angular-momentum-transfer<sup>1-3</sup> (or spin-transfer for short) induced magnetization reversal is a relatively new phenomenon only observed in magnetic structures smaller than 0.1  $\mu\text{m}$  in size.<sup>4-9</sup> It reveals the interaction between magnetization and spin-polarized transport current. The spin-transfer mechanism is further unambiguously observed in recent reports of spin-polarized current induced microwave emission in nano-pillar spin-valve structures.<sup>10,11</sup> This paper give a brief discussion of the behavior of this representative spin-transfer device: namely a [Co|Cu|Co] current-perpendicular (CPP) spin-valve nanopillar.

### 2. FABRICATION METHODS

There are two commonly used fabrication methods for such junction devices. One is the so-called subtractive process, where the relevant multilayered metal film is formed first via vacuum deposition. The pillar-shaped device structure is then formed by selectively etching away portions of the film. Alternatively, the pillar-shaped structure can also be formed via an additive process. Junctions used in this study were fabricated using either a subtractive method<sup>8,12</sup> or a variation of an additive process, namely a batch-fabricated stencil hard-masked substrate approach. The batch fabricated stencil substrate process is used in our lab for the fabrication of current-perpendicular spin-valve structures. Some details of this process has already been published elsewhere.<sup>13,14</sup> To briefly repeat, the process is summarized by Figure 1.

The stencil lip typically is made of 20 nm or so thick platinum. An example of the top stencil structure is shown in Figure 2(a). A typical completed stencil structure would consist of ||10 Ti|100 Cu|1 Ti|50 SiO<sub>2</sub> |1 Ti|20 Pt || (numbers are layer thicknesses in nm).

Send correspondence to: J. Z. Sun.  
E-mail: jmsun@watson.ibm.com, Telephone: 1-914-945-1372.

Exhibit 2

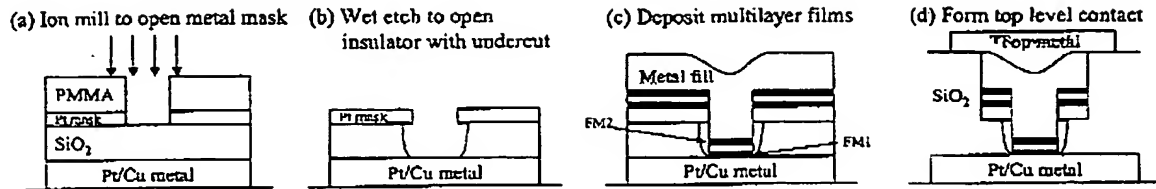


Figure 1. Schematic of the stencil-mask process. (a) E-beam lithography and pattern transfer into the Pt stencil; (b) Wet etch to open up the insulator spacer and creating a controlled amount of undercut; (c) Deposition of magnetic stack followed by metallic filling that gives top electrode contact; (d) Optical lithography for the definition of wiring. Figure reproduced from ref.<sup>14</sup>

CPP junctions for this study have been fabricated using planar magnetron sputter deposition. A typical junction stack consists of  $[[\text{Bottom}|10 \text{ Cu}|3 \text{ Co}|10 \text{ Cu}|12 \text{ Co}|200 \text{ Cu}|10 \text{ Pt}]]$ . A cross-sectional transmission electron microscopy view of the pillar shaped device formed through a stencil structure is shown in Fig.2(b). This cross-section sample is cut from an actual device using focused ion beam.

After deposition of the layers forming the junction device, optical lithography is used to form the necessary bottom and top electrodes so that the current passes through the stencil-defined pillar. For reliable measurements of the junction resistance, the junction resistance needs to be well above the sheet resistance of the electrodes. A bottom electrode made of 100nm copper typically gives a sheet resistance of about 0.08 to 0.1  $\Omega$ , allowing quantitative measurements of junction resistances down to about 1  $\Omega$ .

### 3. QUASI-STATIC TRANSPORT BEHAVIORS

Quasi-static transport measurements were taken in a 4-probe geometry. A dc bias current is applied to the junction. At the same time a small ac current, about 100 $\mu\text{A}$  rms at 331 Hz, is superimposed. The ac voltage is read out through a lock-in setup which measures the dynamic resistance of the junction at the given dc bias current. In what follows unless otherwise specified, all measured junction resistances refer to its dynamic resistance measured using this setup. In a typical quasi-static measurement, the bias current is stepped at a rate around 0.2 to 2 mA/min, while the magnetic field sweep rate (if swept) is on the order of 500-1000 Oe/min.

A typical current-induced magnetic switching loop for a  $0.05 \times 0.15 \mu\text{m}^2$  junction is shown in figure 3(a). Generally speaking, the resistance is hysteretic both in applied field and in bias-current. The values of the switching threshold current  $I_{up}$  and  $I_{down}$  are a function of applied magnetic field and the sample's magnetic and bias-current history.

Figure 4 describes the hysteretic current and field dependence of the junction resistance. Here (a)-(d) are four directions when the bias-current is continuously swept in both directions, while the magnetic field was stepped,

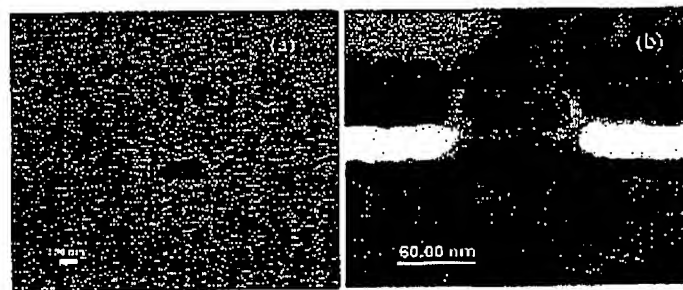


Figure 2. (a) Scanning electron microscopy view of the stencil mask. (b) A transmission electron microscopy cross-sectional image of a pillar device deposited using planar magnetron sputtering.

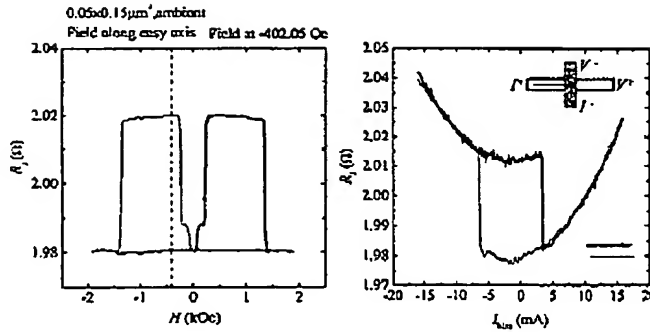


Figure 3. Left: An  $R(H)$  plot of a  $0.05 \times 0.15 \mu\text{m}^2$  junction. Right: A  $R(I)$  plot. Inset shows the arrangement of the leads. Positive direction of current is defined as current flowing from the bottom electrode through the pillar into the top electrode, electrons flow in the opposite direction. Measurement was done at ambient temperature. The vertical dashed line in the left-side panel indicates the bias field at which data for  $R(I)$  were taken.

either up or down, between each bias current sweep. The direction of the current and field sweep is indicated by the arrows on the upper-right corner of each plot. Light color in the contour represents high resistance, dark color, low resistance.

Two different regions can be seen from the data presented in Figure 4. In the low-magnetic field region, the  $R(I)$  sweeps are hysteretic, with  $R(I_{up})$  and  $R(I_{down})$  tracing out a different boundary (subscripts refer to the direction of current sweep). In higher fields, the two branches of boundaries defined by  $R(I_{up})$  and  $R(I_{down})$  converge into a set of reversible bright or dark streaks. These streaks correspond to dynamic resistance peaks or valleys, caused by non-hysteretic steps up or down in the quasi-static  $I-V$  characteristics. Notice the reversible steps only appear in this case in the negative current direction, corresponding to electrons flowing from the thicker cobalt layer into the thinner. When one reverses the order of the thick and thin cobalt layer, the bias-current for these steps changes sign.

The simple zero-temperature mono-domain model as described below for spin-transfer predicts a switching current threshold (albeit a threshold only for instability in the linearized solution of the Landau-Lifshitz-Gilbert equation) of

$$I_c(H) = \left( \frac{2e}{\hbar} \right) \left( \frac{\alpha}{\eta} \right) (abtM_s) (H + H_k + 2\pi M_s) \quad (1)$$

where the applied field  $H$  is along the easy-axis direction as defined by  $H_k$ .  $a$  and  $b$  are the lateral sizes of the

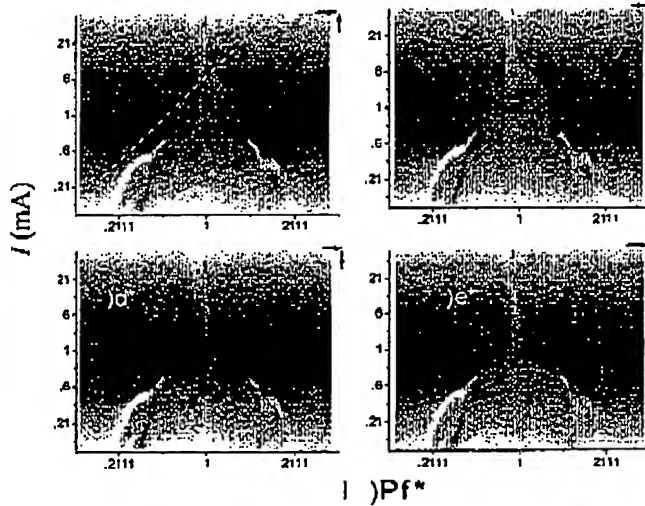


Figure 4. Contour plots of switching boundaries of a  $0.05 \times 0.10 \mu\text{m}^2$  junction. Ambient temperature, field applied along the easy axis direction. The current was swept one full circle at a constant bias field. The bias field was then stepped to the next value. The arrows at the upper right corner of each panel indicate the current sweeping and field stepping direction. The dashed line in (a) indicates the portion of data where the slope-to-intercept ratio were taken for the field-dependent switching current  $I_c(H)$ .

nanomagnet,  $t$  its thickness,  $M_s$  its saturation magnetization.  $\eta$  is the spin-polarization of the current. Eqn.(1) suggests the following relationship in the threshold current's magnetic field dependence:

$$\frac{I_c(0)}{dI_c/dH|_{H=0}} = H_k + 2\pi M_s \quad (2)$$

Namely, it predicts a linear dependence of  $I_c$  on applied field, and the intercept to slope ratio (ISR) of the linear dependence should give  $H_k + 2\pi M_s$ . For cobalt,  $M_s \approx 1,400$  emu/cm<sup>3</sup> at ambient temperature,<sup>15</sup> which would predict an ISR of the order of  $9 \times 10^3$  Oe even if  $H_k \ll 2\pi M_s$ .

A nearly linear dependence of  $I_c$  as a function of applied field  $H$  is indeed observed in a certain range of  $H$ , as shown in Figure 4 (a)-(d), an example is shown in Figure 4(a) by the dashed line. This particular  $I_c(H)$  dependence gives an ISR of only 430 Oe, which is well below the value of close to 9,000 Oe as expected from Eqn.(1). A set of ISRs obtained from various samples is tabulated in Table 1. The experimentally observed values listed in Table 1 systematically fall well below  $4\pi M_s$ . In such measurements the uncertainty of zero-field  $H$  is no larger than the full demagnetization field from the pillar's fixed cobalt layer, whose shape anisotropy (which is the main cause of edge-coupling field) at 120 Å by  $0.05 \times 0.15 \mu\text{m}^2$  is no more than 2.5 kOe (Calculated using, for example, Eqn.(2) in Sun, *et al.*<sup>12</sup>), which is insufficient to account for the discrepancy. It will be shown below that a large contributor to this discrepancy is the effect of finite temperature.

In addition to the simple linear dependence of  $I_c$  on  $H$ , there are regions in the  $(H, I)$  plane where non-hysteric steps were present. Such steps, when measured using the ac-differential method give rise to the sharp peak (or valley, depending on the direction of the step) structure in the observed  $R(H, I)$ , appearing as bright or dark streaks in the contour plot. The detail of these peak width and height depends on the details of sample condition and the ac excitation current amplitude.<sup>14</sup> A detailed analysis of the step width and related peak width and peak height was recently given by Urazhdin *et al.*<sup>16</sup> Alternatively, experimental evidences also exist that suggests the involvement of non-zero- $k$  value spin-wave excitations, with the wavelength of the excited spin-wave mode being simple multiples of the lateral size of the junction pillar.<sup>14</sup> Details of magnetic excitation in this reversible region is likely to be complex, and will depend sensitively on the exact nature of the magnetic boundary conditions of the pillar junction structure.

#### 4. SWITCHING SPEED MEASUREMENT

Direct measurement of the switching speed of spin-transfer junctions is non-trivial because of the small signal level involved. For current-perpendicular (CPP) spin-valves even with lateral sizes reduced to 100nm or below, the junction resistance still is only  $1 \sim 5 \Omega$ , and the magnetoresistance change is even smaller – usually only about about 3 ~ 5 % of total junction resistance. This results in a MR-related voltage signal typically on the order of 0.1 mV. Dynamic calculations<sup>17</sup> give the generic time-scale of the reversal to be around  $(2\pi M_s) \gamma$ , where  $\gamma = 2\mu_B/\hbar$  is the gyro-magnetic ratio, and  $M_s$  is the saturation magnetization of the thin film nanomagnet. This estimate places the switching time on the order of  $1 \sim 10$  ns.

Table 1. A list of measured slope, intercept and ISR for junctions with different size. (†)For comparison, one data-point from the work of Katine *et al.*<sup>8</sup> is also included. Table reproduced from Sun *et al.*<sup>14</sup>

Size ( $\mu\text{m}^2$ )	Slope (A/Oe)	Intercept (mA)	ISR (Oe)
$0.07 \times 0.14$	$6.46 \times 10^{-6}$	7.34	1,136
$0.07 \times 0.14$	$6.39 \times 10^{-6}$	5.87	918.6
$0.05 \times 0.20$	$7.81 \times 10^{-6}$	3.83	490.4
$0.05 \times 0.10$	$8.63 \times 10^{-6}$	7.14	827.3
$0.05 \times 0.10$	$2.82 \times 10^{-6}$	7.81	2,769.5
$0.05 \times 0.10$ (300K)	$1.31 \times 10^{-5}$	5.63	429.8
$0.05 \times 0.10$ (13.4K)	$1.08 \times 10^{-5}$	13.6	1,255
$0.08 \times 0.16$ (300K)	$1.96 \times 10^{-5}$	17.6	898.2
$0.08 \times 0.16$ (13.4K)	$5.98 \times 10^{-5}$	10.8	1,809
$0.06 \times 0.12$ (†)	$2.62 \times 10^{-6}$	3.44	1,314

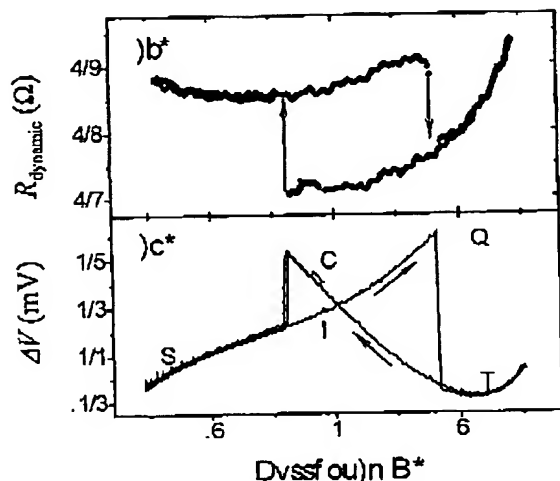


Figure 5. (a) Quasi-static differential resistance of the junction used for switching-speed measurement. (b) Quasi-static I-V characteristics of the junction, with its linear (current-independent) resistance subtracted out. Letters indicate the pulse sequence for high-speed switching measurement, as explained in the text. Figure reproduced from Koch *et al.*<sup>18</sup>

We focus on switching-speed measurements performed at ambient temperature. Fig. 5(a) shows the dynamic resistance of a typical sample used for switching-speed measurements. This particular junction presented here was patterned using a subtractive method.<sup>8</sup> The active film stack sequence for this device is [Co|Cu|Co]. The free layer Co is about 3nm thick, and the lateral junction size is designed to be  $0.05 \times 0.10 \mu\text{m}^2$ . The average resistance for this junction was 3.7 Ohms and the MR resistance change is about 4 percent of the total – a small signal for broad-band measurement with severe common-mode interference from the main excitation current pulse. Additionally, samples often exhibit small changes of junction resistance over the course of a measurement session, perhaps due to contact condition changes. These add a few percent of long-term fluctuation to the measured resistance. To bring out a good broad-band MR signal in such a measurement environment requires a carefully designed multi-trace signal average process.

Figure 5(b) plots the difference between the measured voltage and a straight line vs. the measured current. Details of the measurement has been published by Koch *et al.*<sup>18</sup> To briefly repeat, the measurement was done by alternating two pulse sequences, the "signal" and the "background" sequence. The sample is dc biased at the current at points H (home) or B (background). For the "signal" sequence, a 1 microsecond pulse is applied to place the sample at point R (reset). For current-dependence measurements, a 300 (or sometimes a 30) ns pulse of varying amplitude is applied to place the sample at point P (pulse). If the pulse is sufficiently large, the sample will eventually switch to point S (switched). The voltage across the sample during this sequence is recorded using the TK6500 oscilloscope. The background sequence is taken the same way as the signal except without the reset pulse. When the sample is current pulsed near the switching point, the lack of a reset pulse assures its moving between the two pulse sequences represents the magnetization reversal when the sample is biased between points P and S. Typically 10,000-traces are averaged in groups of 500 signal and background traces.

Figure 6(a) plots the magnetization reversal time for a typical sample as a function of the pulsed current. From there a switching time  $\tau$  can be extracted. That is shown in Fig. 6(b) and (c). Two points are noted for the data shown in Fig. 6(b-c). First, at the high speed limit, the dependence of  $\tau^{-1}$  on bias current  $I$  is linear. Second, in the sub-threshold, large- $\tau$  regime, this linearity gives way to a curved onset which turns out to be exponentially dependent on the bias current as shown in Fig. 6(c). We show below that the linear  $\tau^{-1}$  vs.  $I$  dependence stems from spin-transfer angular momentum conservation, and the curved onset relates to thermal activation. Both can be adequately described by the spin-transfer dynamics with thermal noise. In addition, the threshold current observed in Fig. 6(b) is about 11 mA for the threshold corresponding to the right-side (positive current) step of Fig. 5 which reads only about 4.5 mA. The difference between these two values lie in the vastly different time-scales of the two measurements.

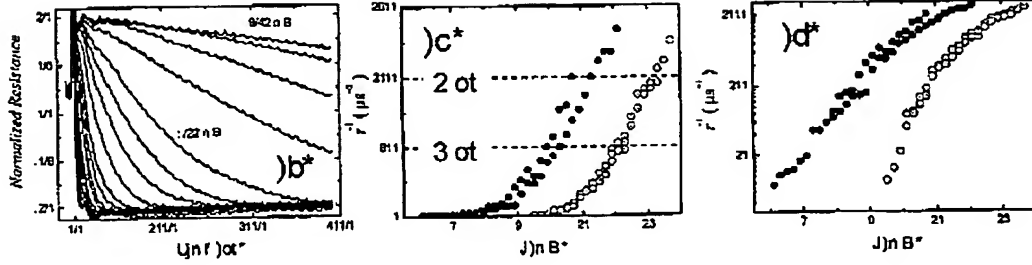


Figure 6. (a) Time-dependent switching probability extracted from measurements illustrated in Fig. 5; (b) Switching speed  $\tau^{-1}$  extracted from (a). Horizontal dashed lines with labels indicate the switching speed corresponding to a reversal time of 1 and 2 nanoseconds, respectively; (c) Switching speed plotted on log-linear scale. Open and closed circle symbols represent the switching threshold on the positive and the negative current step of the junction shown in Fig. 5.

## 5. A MONO-DOMAIN MODEL FOR SPIN-TRANSFER MAGNETO-DYNAMICS

### 5.1. Zero-temperature model

Define a macro-spin with its magnetic moment  $\mathbf{m}$  with a direction described by a unit direction vector  $\mathbf{n}_m = \mathbf{n}_m(\theta, \varphi) = \sin \theta \sin \varphi \mathbf{e}_x + \sin \theta \cos \varphi \mathbf{e}_y + \cos \theta \mathbf{e}_z$  where  $\theta$  and  $\varphi$  are direction angles in a polar coordinate system. The moment  $\mathbf{m}$  is situated in a combined energy potential of  $U = U(\theta, \varphi)$  that includes all energy-conserving torques  $\mathbf{m}$  comes to experience. The normalized gradient of  $U$ , expressed in terms of  $\mathbf{H}_{eff} = (1/m) \nabla U(\theta, \varphi)$  includes terms applied magnetic field  $\mathbf{H}$ , a uniaxial anisotropy whose strength can be characterized by a uniaxial anisotropy field  $H_k$ , and an easy-plane anisotropy field that could be used to describe a macrospin in thin-film geometry, experiencing the demagnetization effect from the flat thin film geometry. Here the operator  $\nabla = \mathbf{e}_\theta (\partial/\partial\theta) + \mathbf{e}_\varphi (1/\sin \theta) (\partial/\partial\varphi)$ , with unit vectors  $\mathbf{e}_\theta$  and  $\mathbf{e}_\varphi$  denoting the direction of rotation for  $\theta$  and  $\varphi$ , respectively. Note that other than the applied field  $\mathbf{H}$ ,  $\mathbf{H}_{eff}$  here is in general not a simple magnetic field vector but would be a function of the angular position of  $\mathbf{m}$ .

The precession dynamics of the macro-spin  $\mathbf{m}$  under potential well  $U$  in the classical limit can be described by the phenomenological Landau-Lifshitz-Gilbert equation:

$$\left(\frac{1}{\gamma}\right) \frac{d\mathbf{m}}{dt} = \mathbf{m} \times \left[ \mathbf{H}_{eff} - \left(\frac{\alpha}{m}\right) \mathbf{m} \times \mathbf{H}_{eff} \right] \quad (3)$$

where  $\gamma = 2\mu_B/\hbar$  is the gyro-magnetic ratio.

Assume a spin-polarized charge current  $I$  flowing along  $\mathbf{e}_x$  direction with spin-polarization along the unit-vector direction  $\mathbf{n}_s$  of the value  $\eta = (I_\uparrow - I_\downarrow)/(I_\uparrow + I_\downarrow)$  (where  $I_\uparrow$  and  $I_\downarrow$  designate current in spin channels parallel and anti-parallel to the direction of  $\mathbf{n}_s$ ). This spin-polarized current is assumed to pass through  $\mathbf{m}$ , being re-polarized by  $\mathbf{m}$  and hence acquiring a new spin-polarization direction  $\mathbf{n}_m$  upon exiting. In this process a certain amount of spin-angular momentum from the spin-polarized current is absorbed by  $\mathbf{m}$ . For realistically achievable current densities and magnetization in metal-based magnetic conductors, it is reasonable to assume the magnitude of  $\mathbf{m}$  will remain unchanged during the process, and hence to the lowest order, only the transverse component of spin-angular momentum deposited into  $\mathbf{m}$  is absorbed by  $\mathbf{m}$ , in the form of a precessional motion for  $\mathbf{m}$ . This is equivalent to adding a new term to Eqn.(3), so the precession dynamics of the macro-spin under the influence of a spin-transfer current will now read

$$\left(\frac{1}{\gamma}\right) \frac{d\mathbf{m}}{dt} = \mathbf{m} \times \left[ \mathbf{H}_{eff} - \left(\frac{\alpha}{m}\right) \mathbf{m} \times (\mathbf{H}_{eff} + \mathbf{H}_s) \right] \quad (4)$$

where  $\mathbf{H}_s = I\eta(\hbar/2e)(1/m\alpha)\mathbf{n}_s$  is the spin-angular momentum transfer term.

To understand the basic physics involved, examine the simple case when only an applied magnetic field  $\mathbf{H}$  is present in  $\mathbf{H}_{eff}$ , and that  $\mathbf{H}$  and  $\mathbf{H}_s$  are collinear. That is, the incoming spin-current has its polarization

aligned (either parallel or anti-parallel) to the direction of the applied field. In this simple limit one may write

$$\left(\frac{1}{\gamma}\right) \frac{d\mathbf{m}}{dt} = \mathbf{m} \times \left[ \mathbf{H} - \left(\frac{\tilde{\alpha}}{m}\right) \mathbf{m} \times \mathbf{H} \right] \quad (5)$$

with  $\tilde{\alpha} = \alpha + \hbar\eta I / (2emH_0) = \alpha(1 + I/I_c)$ , where  $I_c = (2e/\hbar)(\alpha/\eta)(ab\ell M_s)H_0$ , a special case of the threshold current as defined in Eqn.(1). This reveals the role of spin-polarized current  $I$ : it modifies the effective damping coefficient of the nanomagnet. When the effective damping  $\alpha$  becomes negative, the nanomagnet will amplify, rather than damp out, any disturbance away from its equilibrium position, resulting in a magnetic instability leading to a magnetic reversal.

For more general situations, since  $\mathbf{H}_{eff}$  contains the angular position  $(\theta, \varphi)$  of  $\mathbf{m}$ , a full stability analysis of Eqn.(4) is required. This in small cone-angle limit ( $\theta \ll \pi$ ) can be done analytically with a linearized Eqn.(4), as was done in ref.[17]. When averaged over a time-scale longer compared to the natural precession period  $\Omega_K = \gamma H_k$ ,<sup>17</sup> it gives an effective damping coefficient of  $\tilde{\alpha} = \alpha + \hbar\eta I / [2em(H + H_k + 2\pi M_s)]$  that describes the average cone-angle evolution  $\langle \theta(t) \rangle$ . Here an uniaxial anisotropy field  $H_k$  and an orthogonal easy-plane anisotropy term are included. A thin-film demagnetization-related easy-plane anisotropy energy is assumed, therefore  $M_s = m/v$  where  $v$  is the volume of the nanomagnet. The resulting instability threshold, with a uniaxial anisotropy term and an orthogonal easy-plane anisotropy term included is<sup>17</sup>:

$$|I_c| = \frac{1}{\eta} \left(\frac{2e}{\hbar}\right) m\alpha (H + H_k + 2\pi M_s) \quad (6)$$

Notice this threshold current  $I_c(H)$  depends linearly on applied field  $H$ . It should have a intercept-to-slope ratio of  $H_k + 2\pi M_s$ . These can be compared with measurements.

One set of experimentally measured ISR is listed in Table 1. It is immediately apparent that the experimental ISR falls well below the prediction of Eqn.(6). Furthermore, one observes that the ISR measured at a low temperature of 14K appears to show less deviation than those measured at ambient temperature. This suggests that finite temperature effect is at least partially responsible for the discrepancy between the zero-temperature result of Eqn.(6) and experimental observation.

## 5.2. Role of finite temperature

To model the finite temperature environment one follows the approach of Brown *et al.*<sup>19</sup> and Grinstein *et al.*<sup>20</sup> by adding a Langevin random field  $\mathbf{H}_L$  to the effective magnetic field term  $\mathbf{H}_{eff}$ .  $\mathbf{H}_L$  relates to the system temperature  $T$  as  $H_{L,i} = \sqrt{2\alpha k_B T / \gamma m} I_{ran,i}(t)$ , ( $i = x, y, z$ ); where  $I_{ran}(t)$  is a Gaussian random function with the first two moments of  $\langle I_{ran}(t) \rangle = 0$  and  $\langle I_{ran}^2(t) \rangle = 1$ . The  $x, y, z$  components each has its own uncorrelated  $I_{ran}(t)$ . Without the spin-transfer effect the finite temperature LLG equation with a Langevin random field thus reads

$$\left(\frac{1}{\gamma}\right) \frac{d\mathbf{m}}{dt} = \mathbf{m} \times \left[ \mathbf{H}_{eff} + \mathbf{H}_L - \left(\frac{\alpha}{m}\right) \mathbf{m} \times \mathbf{H}_{eff} \right] \quad (7)$$

This describes the dynamics of a macro-spin  $\mathbf{m}$  sitting in a potential well  $U(\theta, \varphi)$ , with a thermally activated motion and a finite lifetime of staying inside the potential well, namely a thermal life-time  $\tau$  approximately following the Boltzmann statistics of

$$\tau = \tau_0 \exp\left(\frac{\Delta U}{k_B T}\right) \quad (8)$$

where  $\Delta U$  is the potential barrier height as seen from the local minimum where  $\mathbf{m}$  fluctuates around, and  $\tau_0 \sim 1/\gamma H_k$  is the reciprocal attempt frequency.  $\Delta U$  can be determined for any given potential landscape  $U(\theta, \varphi)$  and local minimum  $(\theta_0, \varphi_0)$ . This approximation should work well when  $\Delta U/k_B T \gg 1$ . The thermal activation life-time Eqn.(8) is determined once a system is defined by Eqn.(7) and an energy landscape  $U(\theta, \varphi)$ , represented in Eqn.(7) by  $\mathbf{H}_{eff}(\theta, \varphi) = (1/m) \nabla U(\theta, \varphi)$ .

The effect of finite temperature on the macro-spin system's response to a spin-transfer excitation is two fold. First, it affects the average precession motion of the macro-spin by adding thermal activation. Secondly, it adds a thermally distributed initial condition to the macro-spin.

### 5.3. Thermal activation under spin-transfer excitation

Spin-transfer excitation adds an additional torque, thus the zero temperature LLG Eqn.(3) takes on the form of Eqn(4). Similarly, after including the spin-transfer torque, and assume the spin-polarized current does not carry significant entropy flow into the macro-spin system, one can re-write Eqn.(7) to read

$$\left(\frac{1}{\gamma}\right) \frac{d\mathbf{m}}{dt} = \mathbf{m} \times \left[ \mathbf{H}_{eff} + \mathbf{H}_L - \left(\frac{\alpha}{m}\right) \mathbf{m} \times (\mathbf{H}_{eff} + \mathbf{H}_s) \right] \quad (9)$$

with  $\mathbf{H}_s$  representing the spin-transfer-torque related contribution, as defined in Eqn.(4).

Solutions for Eqn(9) in general can only be obtained numerically. It is however instructive to look at the special case when  $\mathbf{H}_s$  and  $\mathbf{H}$  are both collinear to the easy-axis of the uniaxial anisotropy term  $\mathbf{H}_k$  inside  $\mathbf{H}_{eff}$ , and the easy-plane anisotropy is zero. In this case, and for small cone-angle  $\theta \ll 1$ , one can show that  $\mathbf{H}_{eff} = \mathbf{H}_k + \mathbf{H}$ , and hence the effect of  $\mathbf{H}_s$  is simply to modify  $\mathbf{H}_{eff} \rightarrow \tilde{\mathbf{H}}_{eff} = (\mathbf{H}_k + \mathbf{H} + \mathbf{H}_s) \mathbf{n}_s = (\mathbf{H}_k + \mathbf{H}) \left(1 + \frac{H_s}{H_k + H}\right) \mathbf{n}_s = \left(1 + \frac{H_s}{H_k + H}\right) \mathbf{H}_{eff}$ . Thus one can re-write Eqn(9) as

$$\left(\frac{1}{\gamma}\right) \frac{d\mathbf{m}}{dt} = \mathbf{m} \times \left[ \mathbf{H}_{eff} + \mathbf{H}_L - \left(\frac{\alpha}{m}\right) \left(1 + \frac{H_s}{H_k + H}\right) \mathbf{m} \times \mathbf{H}_{eff} \right] \quad (10)$$

Thus one may define  $\tilde{\alpha} = \left(1 + \frac{H_s}{H_k + H}\right) \alpha = (1 + I/I_c) \alpha$ , with  $I_c = (2e/\hbar) (\alpha/\eta) (abtM_s) (H + H_k)$ , another special case of Eqn.(1), and Eqn(10) reverts to Eqn(7)'s form but with  $\alpha$  renormalized by  $\tilde{\alpha}$ :

$$\left(\frac{1}{\gamma}\right) \frac{d\mathbf{m}}{dt} = \mathbf{m} \times \left[ \mathbf{H}_{eff} + \mathbf{H}_L - \left(\frac{\tilde{\alpha}}{m}\right) \mathbf{m} \times \mathbf{H}_{eff} \right] \quad (11)$$

Other than the renormalization of  $\alpha$  to  $\tilde{\alpha}$ , Eqn.(11) is a mathematically equivalent description of a macro-spin system as Eqn.(7) with the same amplitude of  $\mathbf{H}_L$  - assuming the spin current is not by itself introducing additional thermal forces on the macro-spin, which is reasonable as the amount of carriers involved in the passing transport current per unit time is small compared to the equilibrium electron density. This then suggests  $H_{L,i} = H_{L,i} = \sqrt{2\alpha k_B T / \gamma m I_{tan,i}}(t)$  remains valid for this hypothetical macro-spin's LLG equation Eqn(10). However, in Eqn(10) the damping coefficient  $\alpha$  is replaced by  $\tilde{\alpha}$ . To maintain  $H_{L,i}$  therefore it means the macro-spin would see an fictitious temperature  $\tilde{T}$ , such that  $\tilde{\alpha}\tilde{T} = \alpha T$ .

Since Eqn(10) is equivalent to a macro-spin situated at temperature  $\tilde{T}$  with damping  $\tilde{\alpha}$ , one may further deduce that the thermal activation life time of the system can also be expressed in the form of Eqn.(8), except with its temperature re-scaled to  $\tilde{T}$ . That is:

$$\begin{aligned} \tau &= \tau_0 \exp\left(\frac{\Delta U}{k_B \tilde{T}}\right) = \tau_0 \exp\left[\frac{\Delta U}{k_B T} \left(\frac{\tilde{\alpha}}{\alpha}\right)\right] = \\ &= \tau_0 \exp\left[\frac{\Delta U}{k_B T} \left(1 - \frac{I}{I_c}\right)\right] \end{aligned} \quad (12)$$

This conclusion of a linearly current-dependent effective temperature can be directly compared with experiment done in sub-threshold driving current ( $|I| < I_c$ ).

### 5.4. Thermally distributed initial condition

The initial condition of the macro-spin system under spin-transfer excitation is most important when the spin-transfer excitation is large - such as when it is near or exceeding the zero-temperature threshold current  $I_c$ . In this case, when the spin-transfer current is applied suddenly at time  $t_0$ , it will result in a fairly quick magnetic reversal. The switching time required at zero temperature is estimated to be:<sup>17</sup>



$$\begin{aligned}\tau^{-1} &= \frac{\alpha\gamma}{m \ln(\pi/2\theta_0)} (H + H_k + 2\pi M_s) [(I/I_c) - 1] = \\ &= \frac{\eta(\mu_B/e)}{m \ln(\pi/2\theta_0)} (I - I_c), \quad (I > I_c)\end{aligned}\quad (13)$$

Here  $\theta_0$  is the initial deviation of  $\mathbf{m}$  from its easy-axis direction. The second line in Eqn.(13) is essentially a revelation of angular momentum conservation. The first effect a finite temperature brings is an initial deviation  $\theta_0$  with a thermal distribution. Thus the precise switching speed will vary from measurement to measurement. At the same time, the thermal agitation during the course of reversal will add some uncertainty to the exact speed and trajectory of the reversal. This disturbance is likely to be small compared to the large cone-angle motion involved in these reversal events as long as  $\Delta U/k_B T \gg 1$ .

To understand the consequence of a thermally distributed initial  $\theta_0$  one examines a special case with

$$U(\theta, \varphi) = K (\sin^2 \theta + h_p \sin^2 \theta \cos^2 \varphi - 2h \cos \theta) \quad (14)$$

where  $K = mH_k/2$  is the uniaxial anisotropy energy constant,  $h_p = 4\pi M_s/H_k$  is the easy-plane anisotropy field in dimensionless unit, and  $h = H/H_k$  is the applied field, assuming a collinear geometry between  $\mathbf{H}$  and  $\mathbf{H}_k$ . Assume further a small thermal fluctuation amplitude when  $\xi = K/k_B T \gg 1$ . In such limit, the main effect of finite temperature on delay  $\tau$  is through the initial angular position of  $\theta$ :

$$\langle \tau \rangle \approx \left( \frac{m\epsilon}{\eta\mu_B} \right) \left[ \frac{\int_0^{\pi/2} \left( \frac{1}{\theta} \right) \ln \left( \frac{\pi}{2\theta} \right) \exp(-\xi\theta^2(1+h)) \operatorname{erf}(\pi\theta\sqrt{\xi h_p}) d\theta}{\int_0^{\pi/2} \left( \frac{1}{\theta} \right) \exp(-\xi\theta^2(1+h)) \operatorname{erf}(\pi\theta\sqrt{\xi h_p}) d\theta} \right] \frac{1}{(I - I_c)} \quad (15)$$

which in the limit of  $K/k_B T \gg h_p \gg 1$  gives a switching speed based on the ensemble-averaged switching time as:

$$\langle \tau \rangle^{-1} \approx \frac{\eta\mu_B}{m\epsilon} \left[ \frac{\ln(4\pi^2 h_p)}{\pi \ln(K/k_B T)} \sqrt{\frac{1+h}{h_p}} \right] (I - I_c) \quad (16)$$

In this particular limit, switching speed has a current-dependence slope that is directly dictated by thermal activation-induced initial angle. This is only true if there's no transient disturbance fields during the application of the current pulse. Such transient fields would create a sudden rotation of the effective easy-axis direction, and in effect creating a non-zero and non-thermal initial angle  $\theta_0$ , dictating the speed of spin-transfer switch.

Summarizing the temperature-dependence results discussed so far, we conclude:

$$\langle \tau \rangle^{-1} \approx \begin{cases} \tau_0^{-1} \exp \left[ -\frac{K}{k_B T} (1-h)^2 \left( 1 - \frac{I}{I_c} \right) \right], & \text{when } (I \ll I_c) \\ \left( \frac{\eta\mu_B}{m\epsilon} \right) \left[ \frac{\ln(4\pi^2 h_p)}{\pi \ln(K/k_B T)} \sqrt{\frac{1+h}{h_p}} \right] (I - I_c), & \text{when } (I \gg I_c) \end{cases} \quad (17)$$

## 6. COMPARISON OF EXPERIMENTAL DATA WITH MONO-DOMAIN CALCULATIONS

### 6.1. Spin-transfer-switching speed

First, we examine the super-critical region. Experimental data from Fig.6(b) gives for the positive side switching a slope of  $d\tau^{-1}/dI = 1.21 \times 10^{11} (\text{sec} \cdot \text{A})^{-1}$ . According to Eqn.(17), assume spin polarization factor  $\eta = 0.5$ ,  $M_s = 1,400 \text{ emu/cm}^3$  for cobalt, and a nano-magnet size of  $0.05 \times 0.10 \mu\text{m}^2$  in the lateral direction and  $30 \text{ \AA}$  thick, having a magnetization  $m \approx 2.1 \times 10^{-14} \text{ emu}$ , an uniaxial anisotropy field  $H_k \approx 568.6 \text{ Oe}$ , and hence an anisotropy factor  $K = mH_k/2 \approx 5.97 \times 10^{-12} \text{ erg}$  which gives room temperature  $K/k_B T \approx 144$ , and an  $h_p = 4\pi M_s/H_k \approx 30.9$ . The exact value of applied field  $H$  in  $h = H/H_k$  is unknown in the experiment but is

of the order of  $H_k$ , and can be estimated to be  $h \sim 0.5$  from the sub-threshold log-linear slope as is discussed below. With these parameters Eqn.(17) gives  $d\langle\tau\rangle^{-1}/dI \approx (\frac{2\pi k_B T}{\hbar}) \left( \frac{\ln(\frac{K}{k_B T})}{\pi \ln(K/k_B T) \sqrt{1 - I/I_0}} \right) \approx 1.3 \times 10^{11} \text{ (sec.A)}^{-1}$ . This agrees with the experimental value shown in Fig.6(b) to well within a factor of 2.

Next we examine the sub-critical switching region. Details of this analysis is already published by Koch *et al.*<sup>16</sup> To briefly repeat, examine data presented in Fig.6(c). The log-linear dependence of  $\langle\tau\rangle^{-1}$  on current is apparent. The slope of which according to Eqn.(17) gives the strength of the pre-factor  $(1-h)^2 K/k_B T$ , which turns out to be 11.87 and 28.78 for the negative and positive-side switching, respectively.

Thus for the conditions tested experimentally, the functional form of Eqn.(17) adequately describes both the sub- and the super-critical limit of the spin-transfer switching as a function of the switching current amplitude.

### 6.2. Quasi-static switching boundaries and the role of finite temperature

It can now be shown that at finite temperatures, because of thermal activation, the apparent measured quasi-static  $I_0(H)$  will have its intercept-to-slope ratio fall below that of  $H_k + 2\pi M_s$ . To see this recall the sub-critical expression from Eqn.(17). Writing  $\Delta = K/k_B T$ , the relaxation time at a given set of  $(H, I)$  in the  $H-I$  plane is

$$\tau(H, I) = \tau_0 \exp \left[ \Delta (1 - H/H_k)^2 (1 - I/I_0) \right] \quad (18)$$

For an ensemble-averaged time-dependent magnetic moment  $m(t)$  this means

$$\frac{1}{m} \frac{dm}{dt} = -\tau_0^{-1} \exp \left[ -\Delta (1 - H/H_k)^2 (1 - I/I_0) \right] \quad (19)$$

For a time-dependent sweeping measurement of  $m(t)$ , depending on the path of the sweep one can generally write

$$\ln \left( \frac{m_f}{m_0} \right) = -\tau_0^{-1} \int_{(h_0, I_0)}^{(h_f, I_f)} \exp \left[ -\Delta (1 - H/H_k)^2 (1 - I/I_0) \right] \frac{dH}{v_h} \frac{dI}{v_I} \quad (20)$$

where  $v_h = dh/dt$  and  $v_I = dI/dt$  are (generally time-dependent) sweep rate for field and current respectively. The suffixes "0" and "f" denotes the initial and final point of the sweep. Eqn.(20) is a path integral with its value generally dependent on the path between  $(h_0, I_0)$  and  $(h_f, I_f)$ . For example: for  $\Delta \gg 1$ :

$$\frac{m_f}{m_0} \approx \begin{cases} \exp \left\{ \left( \frac{1}{\tau_0 v_I} \right) \frac{\Delta (1 - H/H_k)^2}{\Delta (1 - I/I_0)} \left[ e^{-\Delta (1 - H/H_k)^2 (1 - I/I_0)} - e^{-\Delta (1 - H/H_k)^2} \right] \right\}, & (I\text{-sweep, constant } H) \\ \exp \left\{ \left( \frac{1}{\tau_0 v_h} \right) \frac{\Delta (1 - I/I_0)}{\Delta (1 - H/H_k)^2} \left[ e^{-\Delta (1 - H/H_k)^2 (1 - I/I_0)} - e^{-\Delta (1 - I/I_0)} \right] \right\}, & (H\text{-sweep, constant } I) \end{cases} \quad (21)$$

For large  $\Delta$ , the path-dependence is insignificant. The resulting contour plot of  $m_f/m_0$  as a function of  $(H, I)$  is illustrated by the numerical results in Figure 7. From Fig. 7 it is apparent that at finite  $K/k_B T$  ratio, the apparent switching boundary (as indicated by the dark to bright transition) has a reduced slope-to-intercept ratio as those of zero-temperature  $I_0(H)$ , indicated in Fig.7(a) by the white line above the contour edge. This exercise demonstrates clearly the effect of finite temperature on the reduction of the apparent slope-to-intercept ratio of the quasi-statically measured  $I_0(H)$ . This mechanism is at least partially responsible for the discrepancy between the zero-temperature model prediction and the experimental observation shown in Table 1.

## 7. CONCLUSIONS

Spin-transfer-induced magnetic excitation and magnetic switching is manifested in sub-100nm current-perpendicular spin-valves composed of [Co/Cu/Co] bilayers. The spin-transfer excitation is shown to cause both hysteretic magnetic switching and non-hysteretic magnetic excitation. For magnetic reversal, sub-nanosecond switching speed is experimentally demonstrated. A finite temperature single-domain model is developed to successfully describe the observed magnetic dynamics.

10

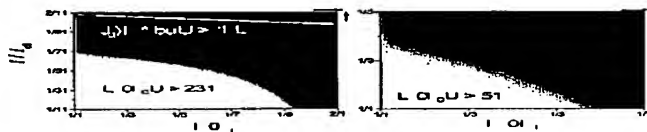


Figure 7. Finite temperature switching probability contour as a function of current and field for two different values of  $K/k_B T$ . Here a constant current sweep rate of  $dI/dt \sim 60 \mu\text{A/sec}$  is used. This contour plot does not look significantly different for a field sweeping approach with  $dH/dt \sim 20 \text{ Oe/sec}$ .

## 8. ACKNOWLEDGMENT

We wish to thank the valuable input from the IBM MRAM team. One of us (JZS) acknowledges a productive collaboration on topics related to this study with B. Oezylmaz and A. D. Kent at New York University supported by NSF-FRG Grant# 0101439.

## REFERENCES

1. J. C. Slonczewski *J. Magn. and Magn. Mat.* 159, p. L1, 1996.
2. L. Berger *Phys. Rev. B* 54, p. 9353, 1996.
3. J. C. Slonczewski *J. Magn. Magn. Mater.* 193, p. L261, 1999.
4. M. Tsai, A. G. M. Jansen, J. Bass, W.-C. Chiang, M. Seck, V. Tsoi, and P. Wyder *Phys. Rev. Lett.* 80, p. 4281, 1998.
5. J. Z. Sun *J. Magn. Magn. Mater.* 202, p. 157, 1999.
6. E. B. Myers, D. C. Ralph, J. A. Katine, R. N. Louis, and R. A. Buhrman *Science* 285, p. 867, 1999.
7. J.-E. Wegrowe, D. Kelly, Y. Jaccard, P. Gütlienne, and J.-P. Ansermet *Europhysics Letters* 45, p. 626, 1999.
8. J. A. Katine, P. J. Albert, R. A. Buhrman, E. B. Myers, and D. C. Ralph *Phys. Rev. Lett.* 84, p. 3149, 2000.
9. J. Grollier, V. Cros, A. Hamzic, J. M. George, H. Jaffrès, and A. Fert *Appl. Phys. Lett.* 78, p. 3663, 2001.
10. S. I. Kiselev, J. C. Sankey, L. N. Krivorotov, N. C. Emley, R. J. Schoelkopf, R. A. Buhrman, and D. C. Ralph *Nature* 425, p. 380, 2003.
11. W. H. Rippard, M. R. Pufall, S. Kaka, S. E. Russek, and T. J. Silva *arXiv:cond-mat/0309042*, 2003.
12. J. Z. Sun, J. C. Slonczewski, P. L. Trouilloud, D. Abraham, I. Bacchus, W. J. Gallagher, J. Hummel, Y. Lu, G. Wright, S. S. P. Parkin, and R. H. Koch *Appl. Phys. Lett.* 78, p. 4004, 2001.
13. J. Z. Sun, D. J. Monma, M. J. Roeks, and R. H. Koch *Appl. Phys. Lett.* 81, p. 2202, 2002.
14. J. Z. Sun, D. J. Monma, T. S. Kuen, M. J. Roeks, D. W. Abraham, B. Oezylmaz, A. D. Kent, and R. H. Koch *J. Appl. Phys.* 93, p. 6859, 2003.
15. C. Kittel, p. 429, *Introduction to Solid State Physics*, 6th Ed. John Wiley & Sons, 1986.
16. S. Urazhdin, N. O. Birge, W. P. P. Jr., and J. Bass *arXiv:cond-mat/0312287v1*, 2003.
17. J. Z. Sun *Phys. Rev. B* 62, p. 370, 2000.
18. R. H. Koch, J. A. Katine, and J. Z. Sun, to appear in *Phys. Rev. Lett.* 2004.
19. W. P. Brown *Phys. Rev.* 130, p. 1677, 1963.
20. G. Grinstein and R. H. Koch *Phys. Rev. Lett.* 90, p. 207201, 2003.

11

Best Available Copy